nature energy

ARTICLES

https://doi.org/10.1038/s41560-021-00817-6

Non-topotactic reactions enable high rate capability in Li-rich cathode materials

Jianping Huang[1], Peichen Zhong[1,2], Yang Ha[3], Deok-Hwang Kwon[1,2], Matthew J. Crafton[4], Yaosen Tian[1,2], Mahalingam Balasubramanian[5], Bryan D. McCloskey[4,6], Wanli Yang[3] and Gerbrand Ceder[1,2] ✉

High-rate cathode materials for Li-ion batteries require fast Li transport kinetics, which typically rely on topotactic Li intercalation/de-intercalation because it minimally disrupts Li transport pathways. In contrast to this conventional view, here we demonstrate that the rate capability in a Li-rich cation-disordered rocksalt cathode can be significantly improved when the topotactic reaction is replaced by a non-topotactic reaction. The fast non-topotactic lithiation reaction is enabled by facile and reversible transition metal octahedral-to-tetrahedral migration, which improves rather than impedes Li transport. Using this concept, we show that high-rate performance can be achieved in Mn- and Ni-based cation-disordered rocksalt materials when some of the transition metal content can reversibly switch between octahedral and tetrahedral sites. This study provides a new perspective on the design of high-performance cathode materials by demonstrating how the interplay between Li and transition metal migration in materials can be conducive to fast non-topotactic Li intercalation/de-intercalations.

The need for novel ideas for Li-ion batteries with high energy and high power is becoming increasingly important as society enters a new electrified era. The operation of a Li-ion battery requires the shuttling of Li^+ ions in and out of electrode materials. To support fast Li transport, a perfect topotactic reaction (in which the host material remains unchanged as its Li content changes) is generally considered crucial because of the minimal disruption to Li transport pathways[1,2]. A topotactic reaction involves reversible Li intercalation into the host structure with only lattice parameter and bond length changes and does not involve diffusive rearrangement of the host atoms[3,4]. In some electrode materials with large capacities, transport of other ionic species besides Li can also occur, leading to a change in the material's structure[5,6]. The transport of multiple ionic species not only increases the kinetic complexities but also affects the Li transport pathways, which is why such non-topotactic reactions are not usually sought after. For example, a large mismatch in the ionic mobilities of the Li and other mobile ionic species can lead to voltage hysteresis[7]. In conversion-type electrode materials (for example, FeF_2, CuF_2, FeOF and Fe_3O_4), sluggish transition metal (TM) or anion migration limits the redox reaction kinetics and induces voltage hysteresis >1 V (ref. [6,8,9]).

The non-topotactic phenomenon is also observed in some intercalation-type electrode materials when TM cations have some mobility. For example, voltage relaxation from 5.2 to 4.5 V occurs in layered $LiNi_{0.5}Mn_{0.5}O_2$ at the top of charge (TOC) because of sluggish Ni migration, and the slow TM motion limits the usable amount of Li that can be inserted at low voltages, thereby resulting in poor rate performance[10,11]. Similarly, poor electrochemical performance in layered $LiCrO_2$ has been attributed to blocked Li diffusion due to Cr migration, even though $LiCrO_2$ shows a high degree of structural similarity to $LiCoO_2$, an extensively commercialized battery electrode material[12,13]. Hence, a general design principle used for high-power cathode materials has been to pursue a perfect topotactic reaction to maintain the structural framework and minimize kinetic complexities. $LiFePO_4$ and spinel $LiMn_2O_4$ are successful examples of this approach. The usefulness of this strategy may have come to an end, as the only cations that have virtually no mobility in dense oxides are those in the currently used $Li(Ni,Mn,Co)O_2$ (NMC) layered oxides, and discovery of new large-capacity cathode materials will require a strategy to manage the mobility of the non-working cations. While polyanion systems are generally better at fixing a metal in place, they tend to have low energy density, and as such are unlikely to spur further improvements in energy density.

In this paper, we present an example in which the Li transport kinetics can be greatly improved when a topotactic reaction is replaced by a non-topotactic reaction, indicating that focusing on fully topotactic intercalation may have led the field to overlook some opportunities for cathode design. We show that in the cation-disordered rocksalt (DRX) $Li_{1.2}Mn_{0.2}Ti_{0.4}Cr_{0.2}O_2$ (LMTC02O), fast Li transport is enabled by facile and reversible Cr octahedral-to-tetrahedral (oct–tet) migration at the TOC, which creates new paths for Li migration. Li-rich DRX materials possess a face-centred cubic (fcc) anion framework with Li transport occurring through a percolation network of Li-rich tetrahedral environments (0-TM channels, where the tetrahedral site does not face-share with any TM)[14,15]. Because Li percolation is supported by the connectivity of available tetrahedral 0-TM channels, any TM occupancy in the tetrahedral site can potentially disrupt such connectivity, and TM migration in DRX materials can be detrimental to Li transport. Surprisingly, we observed that cation-disordered LMTC02O in which most of the Cr has migrated to tetrahedral sites at the TOC shows significantly improved rate performance

[1]Materials Sciences Division, Lawrence Berkeley National Laboratory, Berkeley, CA, USA. [2]Department of Materials Science and Engineering, University of California Berkeley, Berkeley, CA, USA. [3]Advanced Light Source, Lawrence Berkeley National Laboratory, Berkeley, CA, USA. [4]Department of Chemical and Biomolecular Engineering, University of California Berkeley, Berkeley, CA, USA. [5]Advanced Photon Source-X-ray Science Division, Argonne National Laboratory, Argonne, IL, USA. [6]Energy Storage and Distributed Resources Division, Lawrence Berkeley National Laboratory, Berkeley, CA, USA. ✉e-mail: gceder@berkeley.edu

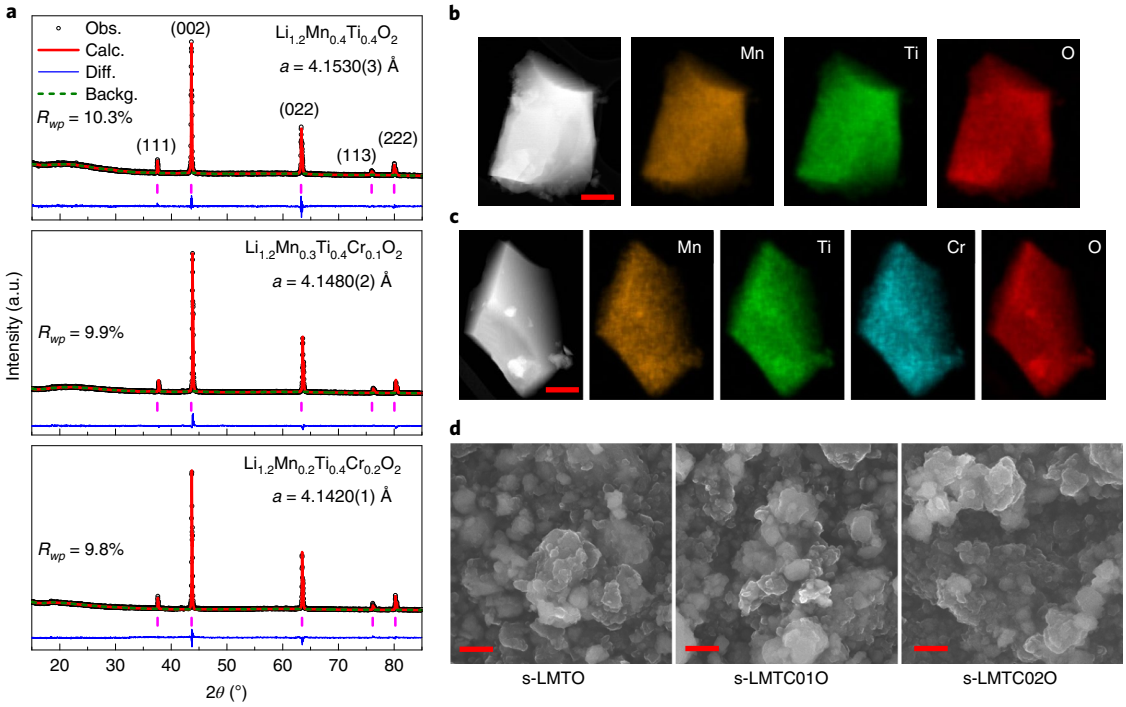

Fig. 1 | Structural characterization of $Li_{1.2}Mn_{0.4-x}Ti_{0.4}Cr_xO_2$. **a**, XRD patterns and refinement results for LMTO, LMTC01O and LMTC02O. Refinement was performed using space group *Fm*-3*m*. Bragg positions are indicated by vertical purple bars. R_{wp}, weighted profile residual. Obs., observed pattern; Calc., calculated pattern; Diff., difference between observed and calculated patterns; Backg., background. **b**,**c**, Transmission electron microscopy (TEM) images (first panel) and EDS mappings (subsequent panels) of LMTO (**b**) and LMTC02O (**c**). Scale bar, 300 nm. **d**, SEM images of shaker-milled LMTO (s-LMTO), LMTC01O (s-LMTC01O) and LMTC02O (s-LMTC02O). Scale bar, 500 nm.

(40% versus 57% capacity reduction when increasing the rate from 20 to 1,000 mA g^{-1}) relative to $Li_{1.2}Mn_{0.4}Ti_{0.4}O_2$ (LMTO), which has no tetrahedral TM upon charging. We demonstrate that the subtle change in the Cr coordination environment redefines the 0-TM Li percolation network at the TOC and increases the percolating Li content, contributing to the high-rate performance. To prove the generalizability of this TM migration concept, we also applied the Cr substitution to a Ni-based DRX system and, similarly, achieved a significant increase in rate performance (160 mAh g^{-1} delivered in 10 min). In contrast to the conventional view of TM migration, our results suggest that the appropriate use of facile TM migration is promising for the design of high-performance cathode materials.

Characterization and electrochemistry of $Li_{1.2}Mn_{0.4-x}Ti_{0.4}Cr_xO_2$

Cation-disordered LMTO, $Li_{1.2}Mn_{0.3}Ti_{0.4}Cr_{0.1}O_2$ (LMTC01O) and LMTC02O were synthesized using a solid-state method. The X-ray diffraction (XRD) patterns of the three samples can be indexed to a disordered rocksalt phase (*Fm*-3*m*) without any apparent impurity peaks (Fig. 1a). The Rietveld refinement results indicate that as Cr substitution increases, the lattice constant decreases, changing from 4.1530 Å for no Cr substitution to 4.1480 Å for LMTC01O and then to 4.1420 Å for LMTC02O, consistent with the smaller ionic radius of Cr^{3+} compared to Mn^{3+}. The scanning transmission electron microscopy (STEM) and energy-dispersive X-ray spectroscopy (EDS) mappings show that elements are uniformly distributed in LMTO (Mn, Ti and O; Fig. 1b) and LMTC02O (Mn, Ti, Cr and O; Fig. 1c). The as-prepared materials were shaker-milled for the electrochemical measurements. Scanning electron microscopy (SEM) images reveal similar particle sizes, ranging from 130 to 200 nm, in the three samples (Fig. 1d).

Galvanostatic cycling at 20 mA g^{-1} between 1.5 and 4.8 V indicates that the $Li_{1.2}Mn_{0.4-x}Ti_{0.4}Cr_xO_2$ samples have similar initial charge and discharge capacities (Fig. 2a,b and Supplementary Fig. 1). LMTO and LMTC02O deliver discharge capacities (energy densities) of 253 mAh g^{-1} (786 Wh kg^{-1}) and 257 mAh g^{-1} (790 Wh kg^{-1}), respectively. Upon increasing the current density from 20 to 1,000 mA g^{-1}, the initial discharge capacity of LMTO decreases to 109 mAh g^{-1} at 1,000 mA g^{-1}. In contrast, the initial discharge capacity of LMTC02O remains at 155 mAh g^{-1} at 1,000 mA g^{-1}. The higher rate capability of LMTC02O is also observed in subsequent cycles (Supplementary Fig. 2). In the voltage window of 4.1–1.5 V, LMTC02O still maintains better rate capability than LMTO (Supplementary Fig. 3).

GITT measurements were used to probe the Li kinetics in $Li_{1.2}Mn_{0.4-x}Ti_{0.4}Cr_xO_2$. The quasi-equilibrium voltage profiles of LMTO and LMTC02O do not display large hysteresis (Supplementary Fig. 4). To calculate the apparent Li diffusion coefficient, we determined the chemical diffusion coefficient from the GITT and divided it by the thermodynamic enhancement factor (Supplementary Note 1 and Supplementary Fig. 5). As the Li content is reduced from $Li_{1.2}TM_{0.8}O_2$ to $Li_{0.6}TM_{0.8}O_2$, LMTO and LMTC02O maintain similar Li diffusion coefficients of 2×10^{-16} to 4×10^{-16} cm^2 s^{-1} (Fig. 2f). However, the apparent Li diffusion coefficient of LMTO decreases by one order of magnitude when more than 0.6 Li per $Li_{1.2}TM_{0.8}O_2$ formula unit is extracted, while such a decrease is not observed in LMTC02O upon charging. Approximately one Li per formula unit can be extracted from LMTC02O with a reasonable Li diffusion coefficient ($>2\times10^{-16}$ cm^2 s^{-1}), indicating that LMTC02O has improved Li kinetics relative to LMTO at the TOC. The improved Li kinetics of LMTC02O upon charging contribute to its improved rate performance relative to LMTO, which is further supported by electrochemical impedance spectroscopy (Supplementary Note 2 and Supplementary Fig. 6) and cyclic voltammetry (Supplementary Note 3 and Supplementary Fig. 7) results. Note that the actual diffusion coefficient depends on an approximation for the active surface

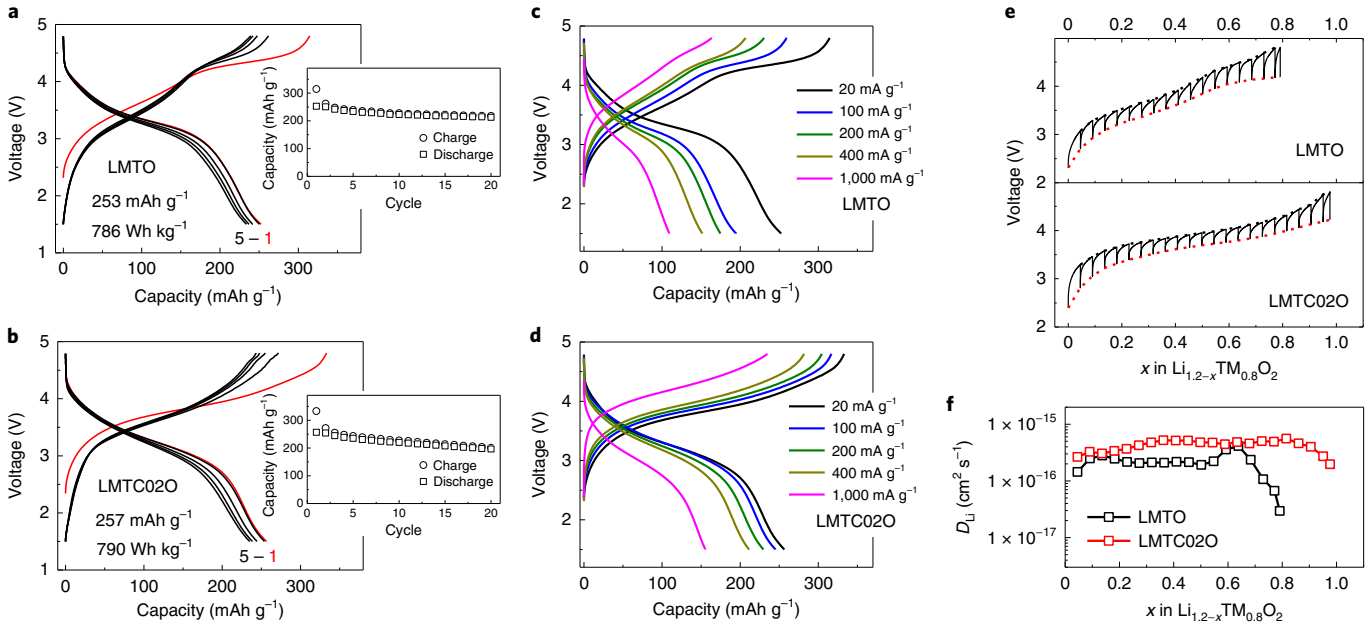

Fig. 2 | Electrochemistry of $Li_{1.2}Mn_{0.4-x}Ti_{0.4}Cr_xO_2$ at room temperature. a,**b**, Voltage profiles of LMTO (**a**) and LMTC02O (**b**) at 20 mA g^{-1} in the voltage window of 4.8–1.5 V. The voltage profiles of cycle 1 are plotted as red lines and the voltage profiles of cycles 2–5 are plotted as black lines. The insets show the capacity retention of the samples over 20 cycles. **c**,**d**, First-cycle voltage profiles of LMTO (**c**) and LMTC02O (**d**) at different current densities. **e**, Voltage profiles of LMTO and LMTC02O under galvanostatic intermittent titration technique (GITT) mode. The voltage profiles are plotted as black lines, the voltages at the beginning of each relaxation step are plotted as black dashed lines and the quasi-equilibrium voltages are plotted as red dashed lines. **f**, Apparent Li diffusion coefficients of LMTO and LMTC02O calculated from the GITT results.

area; however, this uncertainty does not affect the relative variations with Li content.

Redox mechanism and structural change

Hard X-ray absorption spectroscopy (XAS) and soft X-ray mapping of resonant inelastic X-ray scattering (mRIXS) were used to analyse the TM and oxygen redox, respectively, in LMTO and LMTC02O (Fig. 3a–e). Mn K-edge X-ray absorption near edge structure (XANES) spectra reveal that both LMTO and LMTC02O undergo Mn^{3+}/Mn^{4+} oxidation when charged to 4.8 V (Fig. 3a,b). Upon discharging to 1.5 V, the XANES spectra of LMTO and LMTC02O almost recover to those of the pristine states, indicative of the reduction of Mn^{4+} to Mn^{3+}. A prominent pre-edge component in the Cr K-edge XANES is a characteristic feature of Cr^{6+}, which is attributed to a $1s \rightarrow 3d$ transition. Comparison of the pre-edge intensities in the Cr K-edge XANES spectra[16] of the CrO_3 standard and the 4.8 V-charged LMTC02O provides strong evidence that Cr^{3+} in LMTC02O is fully oxidized to Cr^{6+} (Fig. 3c). The prominent pre-edge feature disappears as LMTC02O is discharged to 1.5 V, indicating that the Cr^{3+}/Cr^{6+} redox is mostly reversible. Ti K-edge XANES indicates that Ti^{4+} in LMTO and LMTC02O is not redox-active within the applied voltage window (Supplementary Fig. 8).

The oxidation of lattice oxygen was probed using O K-edge mRIXS, which has been shown to be a robust technique for detecting the oxidized lattice oxygen in battery cathodes[17,18]. It has been established in many oxygen redox systems that an mRIXS feature around 531 eV excitation and 523.7 eV emission energies will emerge when the electrode is charged, indicating oxidized oxygen in the charged state[17,18]. Indeed, the O K-edge mRIXS shows this characteristic feature of oxidized lattice oxygen in the 4.8 V-charged LMTO (Fig. 3d) and 4.8 V-charged LMTC02O (Fig. 3e), indicating the oxidation of lattice oxygen upon charging. Differential electrochemical mass spectrometry (DEMS) analysis revealed minor O_2 gas evolution upon charging in both LMTO and LMTC02O, suggesting a small amount of irreversible oxygen oxidation (Supplementary Fig. 9). This O-release is common in DRX cathodes but is generally smaller than in high-Ni layered cathodes[19,20]. The observed CO_2 evolution may originate from the oxidation of residual lithium carbonate or the carbonate solvents, as shown in prior studies[21,22].

The ex situ XRD patterns indicate that the bulk structural change in LMTO and LMTC02O is reversible upon charging and discharging (Supplementary Fig. 10). The lattice constants decrease by only 1.4% (LMTO) and 1.0% (LMTC02O) after charging to 4.8 V and almost recover to those of the pristine state after discharging to 1.5 V, mirroring the very small volume changes seen in some DRX materials[14,15]. The local structural changes were characterized using EXAFS spectroscopy. In the Cr K-edge EXAFS spectra, the peaks at ~1.0, ~1.5 and ~2.5 Å correspond to the tetrahedral Cr–O, octahedral Cr–O and Cr–TM coordinations, respectively. The EXAFS fitting reveals that in the pristine state of LMTC02O, all of the Cr resides in octahedral sites (Cr_{oct}) with a Cr–O bond distance of ~1.98 Å (Fig. 3f and Supplementary Table 1). The majority of the Cr (99 ± 9%) migrated to tetrahedral sites (Cr_{tet}) in the 4.8 V-charged state, and the Cr–O bond distance decreased to ~1.63 Å. Most of the tetrahedral Cr reversibly migrated back to the octahedral sites upon discharging to 1.5 V (Supplementary Note 4 and Supplementary Fig. 11). The occupation of Mn and Ti in the tetrahedral sites was not observed in LMTO or LMTC02O (Supplementary Fig. 12), confirming that Mn^{3+} (Mn^{4+}) and Ti^{4+} prefer the octahedral sites.

Discussion

Li diffusion in rocksalt-like oxides occurs by octahedral–tetrahedral–octahedral (oct–tet–oct) jumps[23,24]. Although in layered cathode materials these Li jumps are confined to the two-dimensional Li slab, in DRX materials they occur through the statistically percolating network of tetrahedral sites that have no face-sharing TM (0-TM)[14,25]. Thus, an increase in the amount and connectivity of

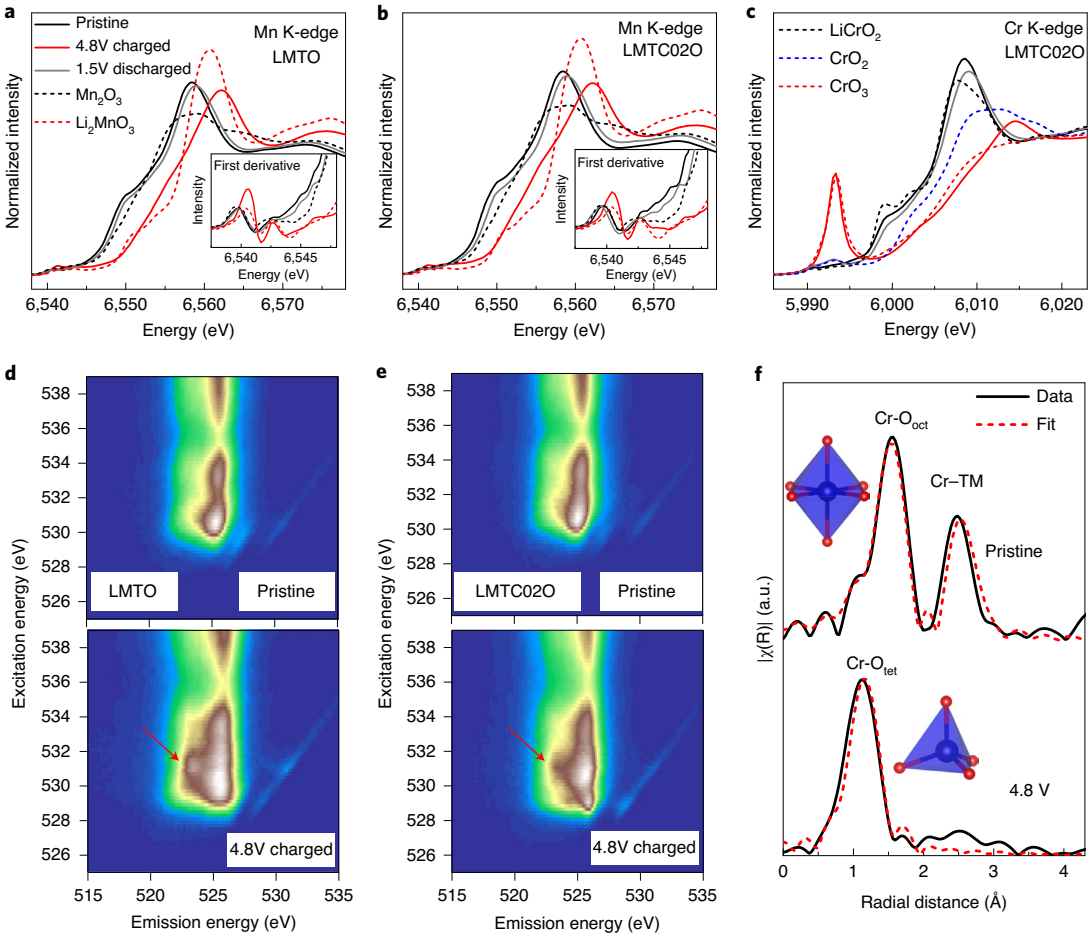

Fig. 3 | Redox mechanism and structural change of $Li_{1.2}Mn_{0.4-x}Ti_{0.4}Cr_xO_2$. a,b, Mn K-edge XANES spectra of LMTO (**a**) and LMTC02O (**b**) in pristine, 4.8 V-charged and 1.5 V-discharged states. The Mn_2O_3 and Li_2MnO_3 standards spectra are plotted as dashed lines. The insets show the first derivatives of normalized absorbance in the pre-edge regions of the Mn K-edge XANES spectra. **c**, Cr K-edge XANES spectra of LMTC02O in pristine, 4.8 V-charged and 1.5 V-discharged states. The $LiCrO_2$, CrO_2 and CrO_3 standards spectra are plotted as dashed lines. **d**,**e**, O K-edge mRIXS of LMTO (**d**) and LMTC02O (**e**) in pristine and 4.8 V-charged states. **f**, Fitted Cr K-edge extended X-ray absorption fine structure (EXAFS) spectra of LMTC02O in pristine and 4.8 V-charged states. The fitting was performed in the radial distance range of 1 to 3 Å using Cr–O and Cr–TM single scattering paths. The peaks at ~1.0, ~1.5 and ~2.5 Å correspond to the tetrahedral Cr–O ($Cr\text{–}O_{tet}$), octahedral Cr–O ($Cr\text{–}O_{oct}$) and Cr–TM coordinations, respectively. The insets show the octahedral CrO_6 and tetrahedral CrO_4 coordinations. |χ(R)|, magnitude of Fourier transformed EXAFS.

0-TM tetrahedra is conducive to improving the Li kinetics in DRX materials. Figure 4a illustrates how occupation of an octahedral site by a TM inhibits Li migration through the eight tetrahedral sites it shares a face with. If this octahedral TM moves into a neighbouring tetrahedral site (Fig. 4b), it creates seven potential new 0-TM channels, depending on the occupancy of the other octahedra these tetrahedra face-share with. Two specific conditions are required for a TM to migrate to a tetrahedral site: (1) a tetrahedral site can only be occupied when its face-sharing octahedral sites are empty, which is more likely near the TOC where Li tri-vacancies can form, and (2) the TM has to prefer four-fold over six-fold coordination, which preference is determined by its electronic structure and size[26]. As shown by the XAS results, Cr^{6+} forms in the charged state, which, with its d^0 electronic configuration and small ionic radius in the tetrahedral site (0.26 Å according to Shannon[27]) is likely to favour the tetrahedral site. The tri-vacancy condition for the migration event allow us to partially characterize the environment of the tetrahedral sites around the octahedral site that is vacated by TM migration, as shown in Fig. 4b. Three of the tetrahedra face-share with at least two octahedral vacancies (2-V_a tetrahedra; green circles in Fig. 4b), and four tetrahedra have one octahedral vacancy guaranteed (1-V_a tetrahedra; yellow circles in Fig. 4b). The 2-V_a and 1-V_a tetrahedra become 0-TM channels if the other face-sharing octahedral sites are occupied by a Li (or by a vacancy, at later stages of delithiation). As 60% of the octahedral sites are occupied by Li in $Li_{1.2}TM_{0.8}O_2$, the 2-V_a tetrahedra have a 36% (0.6×0.6) possibility of being a 0-TM channel, and the 1-V_a tetrahedra have a 21.6% (0.6×0.6×0.6) possibility of being a 0-TM channel, assuming a random cation distribution. Therefore, Cr migration will generate on average ~2 (0.36×3+0.216×4) new 0-TM channels out of the eight tetrahedral sites. This demonstration shows that TM oct–tet migration in a disordered rocksalt-type structure is likely to create additional Li transport pathways, leading to better Li kinetics.

In an actual DRX material, cation short-range order affects the overall cation distribution, which determines the amount and connectivity of the 0-TM channels[28]. To model this more realistic condition, we performed cluster-expansion Monte Carlo simulations to investigate the changes in Li percolation by Cr oct–tet migration in the presence of short-range order (Fig. 4c,d). Monte Carlo simulations were performed at 1,273 K, with 1,000 Monte Carlo representative structures sampled from the equilibrium ensemble. In the pristine (discharged) state, ~36% of all Li ions were found to be part

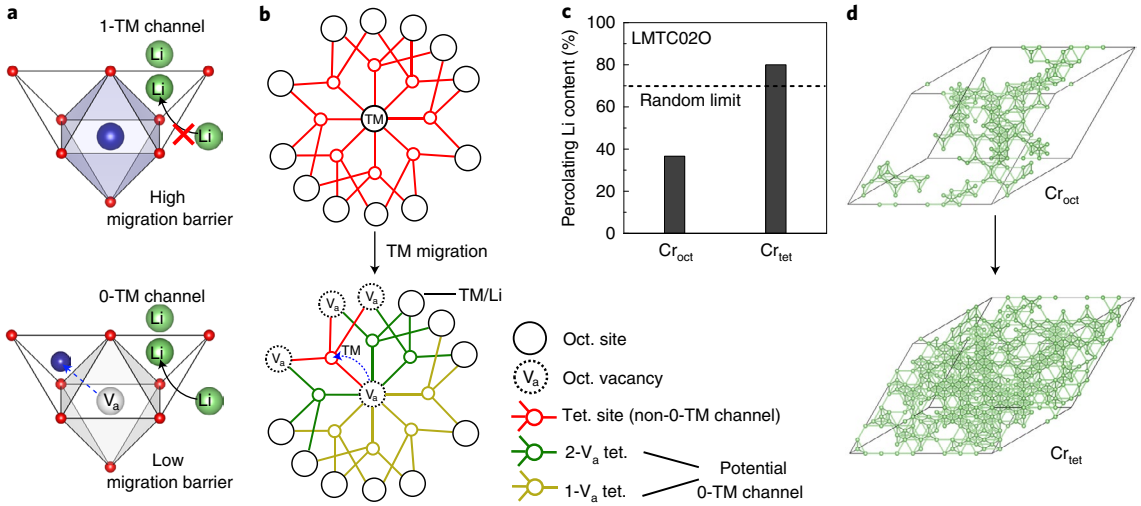

Fig. 4 | Effect of TM migration on Li kinetics. a, Illustration of a TMO_6 octahedron with two face-sharing tetrahedral sites. Migration of the TM from the octahedron transforms a 1-TM channel (a tetrahedral site with one face-sharing octahedral TM) into a 0-TM channel. **b**, Illustration of Li-pathway availability in a rocksalt-type structure before and after TM migration. The structure shows an octahedral TM that is connected to eight tetrahedral sites. The presence of the TM in the octahedral site makes all eight tetrahedral sites non-0-TM channels (red circles). After the TM migrates to a tetrahedral site, the other seven tetrahedral sites become potential 0-TM channels (green or yellow circles), depending on the cations in the other nearby octahedra. **c**, Calculated percolating Li content via 0-TM channel in LMTC02O when Cr occupies octahedral sites (Cr_{oct}) in the pristine state and tetrahedral sites (Cr_{tet}) after possible migration. The dotted line shows the percolating Li content via the 0-TM channel in the random structure limit. **d**, Representative Monte Carlo-simulated structures for LMTC02O with octahedral Cr and tetrahedral Cr. Li atoms are shown as green spheres, and 0-TM connected Li are bridged with green lines.

of the 0-TM percolating network in LMTC02O, about the same as for LMTO (ref. [28]). To reveal how Cr migration modifies the percolating Li content, we first investigated whether Cr migration is energetically favourable upon delithiation. We compared the energies of Cr_{oct} and Cr_{tet} in the presence of a tri-Li vacancy (Methods) and found that migration of Cr to the tetrahedral sites lowers the energy by ~0.3 eV, with reasonable migration barriers (Supplementary Note 5 and Supplementary Fig. 13), indicating feasible Cr migration to the tetrahedral site. We found that in the Monte Carlo configurations sampled at 1,273 K, 87% of the Cr was in an environment where it would be able to migrate to a near-neighbour tetrahedral site upon delithiation in LMTC02O. As a result of this migration, ~80% of the Li sites become part of the 0-TM network, which more than doubles the amount of Li that is part of the percolating migration path. Overall, it is remarkable how this subtle change in the Cr coordination environment redefines the Li percolation network, leading to improved Li kinetics.

Extension to other systems

To verify the generalizability of this concept to other DRX materials, we also studied a Ni-based system by comparing the rate behaviour of cation-disordered $Li_{1.2}Ni_{0.2}Ti_{0.6}O_2$ (LNTO) with that of $Li_{1.2}Ni_{0.1}Ti_{0.5}Cr_{0.2}O_2$ (LNTC02O). The XRD patterns and TEM results indicate that Cr was successfully introduced into the bulk structure of LNTC02O (Fig. 5a,b and Supplementary Fig. 14). The rate performance of the Cr-substituted sample is considerably higher than that of the non-substituted sample, even though the amount of Ni redox is decreased. Whereas LNTO only retains 30% of its capacity (falling from 216 to 64 mAh g^{-1}) upon increasing the current density from 20 to 1,000 mA g^{-1}, LNTC02O retains 60% (falling from 271 to 160 mAh g^{-1}) for the same current increase (Fig. 5c). Upon electrochemical cycling at 1,000 mA g^{-1}, LNTC02O maintains a reversible capacity of 110 mAh g^{-1} for 100 cycles (Fig. 5d). In the voltage window of 4.3–1.5 V, the $Li_{1.2}Ni_{0.2-x}Ti_{0.6-x}Cr_{2x}O_2$ samples all showed reasonable capacity retention with <0.3% capacity fade per cycle, and LNTC02O maintained a capacity >184 mAh g^{-1} for 50 cycles at 20 mA g^{-1} (Supplementary Fig. 15). The apparent Li diffusion coefficients determined from GITT (Supplementary Fig. 16) indicate similar Li kinetics in LNTO and LNTC02O during the initial delithiation process (x in $Li_{1.2-x}TM_{0.8}O_2$ is <0.3) (Fig. 5e). When more Li is removed, the diffusion coefficient in LNTO decreases continuously to ~1×10^{-17} cm^2 s^{-1}, whereas diffusivity of lithium in LNTC02O remains at ~1×10^{-16} cm^2 s^{-1} for the full range of 1 Li^+ per formula unit extraction. The faster Li kinetics of LNTC02O in the highly delithiated state can be attributed to the formation of tetrahedral Cr^{6+} during the charge process (Fig. 5f, Supplementary Note 6 for the redox mechanism and Supplementary Figs. 17–19), consistent with the Cr-substituted Mn-based samples. RIXS spectra also reveal oxygen oxidation in both the LNTO and LNTC02O samples, as evidenced by the peak at the emission energy of 523.7 eV (ref. [17]) (Fig. 5g and Supplementary Fig. 18). The peak feature of oxidized oxygen disappeared when LNTO/LNTC02O was discharged to 1.5 V, indicating a reversible reduction of the oxidized oxygen.

We believe that this non-topotactic behaviour is also responsible for the reported performance of some other DRX materials. A relatively low percolating Li content (<15%) has been predicted in some V-based DRX materials ($Li_{1.2}V_{0.6}Nb_{0.2}O_2$ and $Li_{1.2}V_{0.67}Mo_{0.13}O_2$) (ref. [28]), which appears to be somewhat inconsistent with the good performance of these materials, as disordered $Li_{1.25}V_{0.5}Nb_{0.25}O_2$ (ref. [29]) delivers initial charge/discharge capacities of 250 mAh g^{-1}, corresponding to 67% Li utilization. The prominent pre-edge feature in the V K-edge XANES spectra[29] implies the presence of tetrahedral V^{5+} in the charged state, although detailed V–O bond analyses (for example, V K-edge EXAFS) would be required to unambiguously confirm this. But it appears likely that, as in the Cr-doped systems, V^{5+} migration to tetrahedral sites improves the Li diffusion network and hence the kinetics of this material as it is being charged.

Our experimental and theoretical results indicate that non-topotactic delithiation can improve the Li kinetics. The rate performance of both Mn- and Ni-redox-based DRX materials is significantly improved by the addition of Cr. Further support for the benefits of Cr migration on the Li kinetics is the lack of any drop

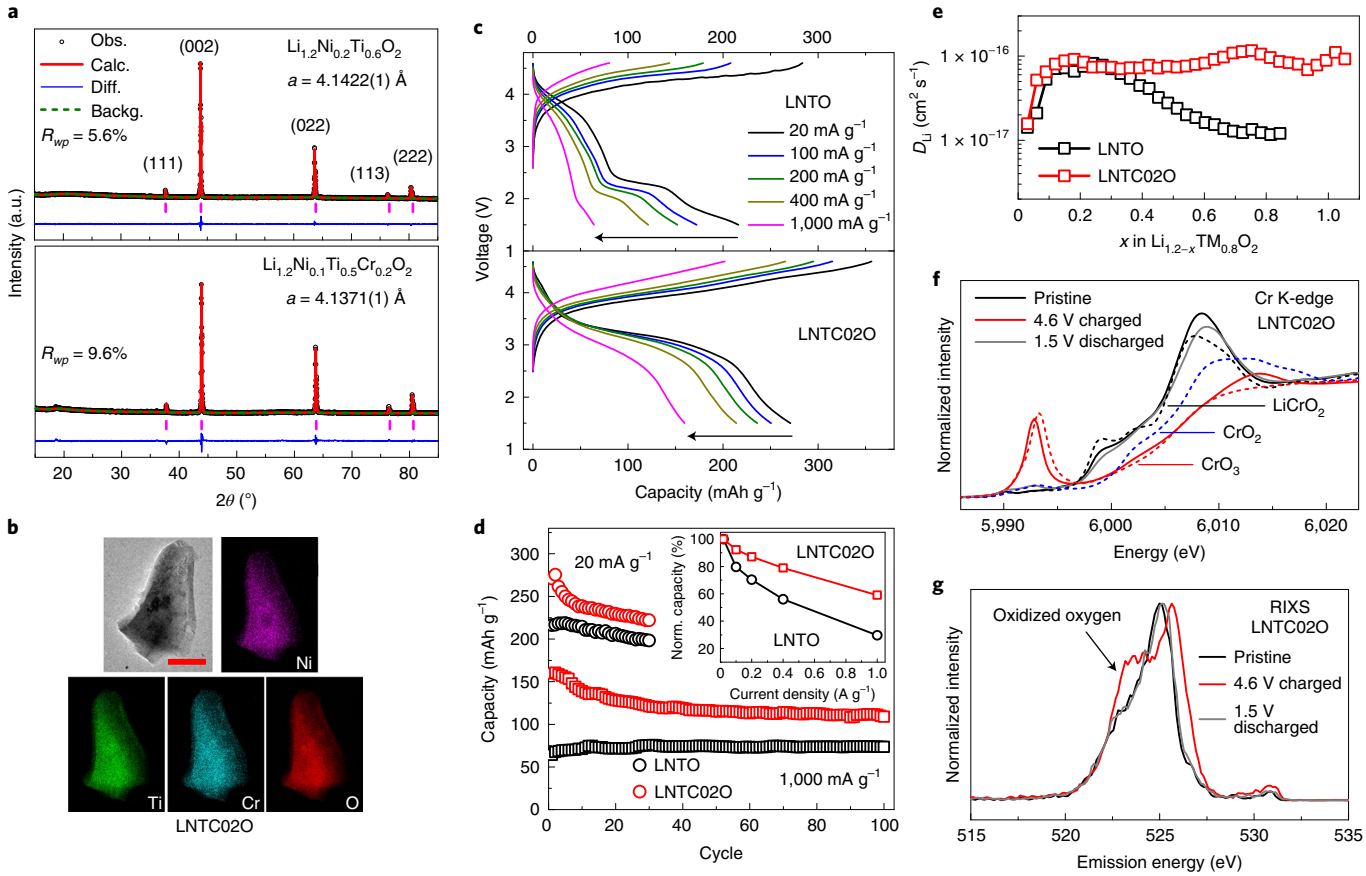

Fig. 5 | Structural characterization and electrochemistry of $Li_{1.2}Ni_{0.2-x}Ti_{0.6-x}Cr_{2x}O_2$. **a**, XRD patterns and refinement results for LNTO and LNTC02O. Refinement was performed using space group *Fm*-3*m*. Bragg positions are shown by vertical purple bars. **b**, TEM image (first panel) and EDS mappings (subsequent panels) of an LNTC02O particle. Scale bar, 200 nm. **c**, First-cycle voltage profiles of LNTO and LNTC02O at different current densities in the 4.6–1.5 V voltage window. The black arrows indicate increasing current density. **d**, Capacity retention of LNTO and LNTC02O at 20 and 1,000 mA g^{-1} in the 4.6–1.5 V voltage window. The inset shows the normalized capacity as a function of current density. **e**, Apparent lithium-ion diffusion coefficients of LNTO and LNTC02O calculated from the GITT results. **f**, Cr K-edge XANES spectra of LNTC02O in pristine, 4.6 V-charged and 1.5 V-discharged states. The XANES spectra of $LiCrO_2$, CrO_2 and CrO_3 standards are plotted as black, blue and red dashed lines, respectively. **g**, O L-edge RIXS spectra of LNTC02O collected at an excitation energy of 531 eV. The peak at an emission energy of 523.7 eV is a characteristic feature of oxidized oxygen.

in the measured Li diffusivity in the Cr-doped samples, whereas undoped samples see reduced diffusivity after about 100 mAh g^{-1} (LNTO) and 200 mAh g^{-1} (LMTO). These results are consistent with the ab initio computed driving force for Cr to migrate to tetrahedral sites near the TOC and the geometric analysis showing that TM migration produces an increase in lithium pathways. The rate performance of the Cr-doped materials is comparable to that of state-of-the-art Li-rich cathodes, such as doped $Li_{1.2}Ni_{0.2}Mn_{0.6}O_2$, Li-rich NMC and Li_2RuO_3-based materials (Supplementary Table 2)[30–33] despite the presence of oxygen oxidation (RIXS results). Some recent studies on Li-rich layered cathodes have shown that the oxidized oxygen species are stabilized by metal–oxygen decoordination, which requires TM migration[34]. It is possible that the Cr oct–tet migration in DRX materials creates such a metal–oxygen decoordination, thereby limiting its ability to degrade the rate.

Our results may force a rethinking of the conventional view that TM migration is an unfavourable phenomenon that impedes Li transport and increases hysteresis[7–10]. We now discuss in more detail the specific requirements for non-topotactic changes to improve kinetics, first with a focus on the Cr-doped DRX systems and then in the broader context of cathode materials.

The TM is the main obstacle for the diffusion of Li because its electrostatic repulsion dominates the energy in the activated state[23,24,35]. From this perspective, displacement of some TMs to tetrahedral sites is obviously favourable as it clears multiple oct–tet–oct paths from neighbouring TMs, lowering the barrier for lithium to migrate through them, as our analysis in Fig. 4b shows. Migration of a TM from an octahedral to a tetrahedral site is enabled by an appropriate electronic configuration and ionic size. While d^3-Cr^{3+} has a strong preference for octahedral occupancy, the oxidized d^0-Cr^{6+} has no ligand field stabilization in the octahedral site. Other electronic configurations such as d^5 and d^{10} are also favourable for TM migration to the tetrahedral site[26]. Another contributing factor for facile TM migration is the match between the TM size and the tetrahedron height. For example, a tetrahedron height of 2.39 Å (centroid–vertex distance of 1.79 Å) is large enough for a tetrahedral Cr–O bond (1.64 Å (ref. [27])) but too small for a tetrahedral Ti–O bond (1.80 Å (ref. [27])). As a result, d^0-Cr^{6+} migrates to the tetrahedral site while d^0-Ti^{4+} remains octahedral. In some layered cathodes with larger tetrahedron heights (~2.56 Å), oct–tet migration of Ti^{4+} does occur[36], showing that both the electronic configuration and ionic size requirements need to be satisfied to enable TM migration.

While our focus has been on non-topotactic Li-cycling in DRX materials, we highlight a set of more general conditions that may have to be satisfied in order for non-topotactic behaviour not to impede transport. (1) The non-topotactic processes should be fast and reversible. Slow processes will cause hysteresis, which reduces the discharge energy. As only a few atomic hops may be

required for the non-topotactic process, atomic migration processes with activation barrier below 1 eV are relevant. In our example of Cr-substituted DRX materials, a single hop from an octahedral site to a tetrahedral site is all that is needed to improve Li kinetics. (2) If possible, the non-topotactic processes should be non-cooperative. Large-scale coordinated processes tend to have a high activation energy and will almost certainly lead to hysteresis. This requirement exemplifies one advantage of DRX materials. Because of their disordered nature, the oct–tet TM migration at a specific site occurs independently of the migration at other sites, essentially creating a set of randomly oriented strain dipoles. This is in stark contrast with layered materials that have oct–tet migration, such as $LiCrO_2$ (ref. [13]), where preferential migration of Cr into the tetrahedral site in the Li layer creates a much more cooperative transition.

It may be possible to improve layered oxides as well by enabling non-topotactic phenomena. Near the TOC, layered materials experience a large contraction of slab spacing that reduces the Li mobility. The presence of other cations in the slab can mitigate this contraction by acting as a 'pillar' and increase Li mobility at TOC. However, in the discharged state small high-valent ions usually contract the slab space too much, reducing the discharge kinetics. The difference in performance this leads to can be seen by, for example, comparing solid-state synthesized $Li(Ni_{0.5}Mn_{0.5})O_2$, which has considerable Ni in the Li slab, with ion-exchanged $Li(Ni_{0.5}Mn_{0.5})O_2$ (refs. [1,10,37]), which has almost no Ni in the Li layer. An ion that would move to the Li slab at TOC and move back into the TM layer at the end of discharge would improve kinetics at both charge and discharge. Other non-topotactic but reversible metal migrations have been observed in Mg intercalation electrochemistry[38]. While the use of Cr in commercial cathodes may raise some issues concerning its strong oxidizing character and toxicity, appropriate engineering controls at the electrode/cell level (for example, surface coating and battery recycling) should help reduce these potential hazards, similarly to engineering controls implemented in the lead-acid battery industry. In addition, it may be possible to mimic the Cr effect with other TMs (for example, V^{5+}, Mo^{6+}, Fe^{3+} or Mn^{2+}) that can undergo oct–tet migration.

In conclusion, we demonstrated significantly improved rate performance in cation-disordered rocksalt cathodes due to a non-topotactic reaction, which stands in contrast to the conventional view that fast Li transport is favoured by perfectly topotactic systems. In our example, the fast non-topotactic reaction is enabled by reversible TM migration between the oct and tet sites, which improves the Li diffusion network by creating additional Li transport pathways. We believe that well-engineered non-topotacticity provides a new opportunity to design high capacity cathode materials.

Methods

Synthesis. $Li_{1.2}Mn_{0.4-x}Ti_{0.4}Cr_xO_2$ and $Li_{1.2}Ni_{0.2-x}Ti_{0.6-x}Cr_{2x}O_2$ were synthesized using a solid-state method. Li_2CO_3, Mn_2O_3, $NiCO_3$, TiO_2 and Cr_2O_3 were used as precursors, with 5% excess Li_2CO_3. The precursors were mixed in ethanol and ball-milled for 15 h. The mixture was then dried and pelletized. To prepare LMTO, LMTC01O and LMTC02O, the precursor mixtures were heated for 10 h under argon at 1,000 °C, 1,000 °C and 1,050 °C, respectively. To prepare LNTO and $Li_{1.2}Ni_{0.15}Ti_{0.55}Cr_{0.1}O_2$, the precursor mixtures were heated at 1,000 °C for 3 h in air. To prepare LNTC02O, the mixture was heated at 1,050 °C for 10 h in air.

Electrochemistry. The active material, carbon black (Timcal, SUPER C65) and polytetrafluoroethylene (PTFE, DuPont, Teflon 8A) were mixed at a weight ratio of 70:20:10 to prepare the cathode film. First, 210 mg of the active material and 60 mg of carbon black were mixed and shaker-milled for 1 h in an argon atmosphere using a SPEX 800 M mixer; next, PTFE was added to the mixture, which was then manually mixed for 30 min. The three components were rolled into a thin film inside an argon-filled glove box. The electrolyte used was 1 M $LiPF_6$ in a 1:1 (volume ratio) mixture of ethylene carbonate and dimethyl carbonate (BASF). Coin cells were assembled using the cathode film, lithium-metal foil, the electrolyte and separators (Whatman glass microfibre filter) in an argon-filled glove box. The loading density of active material was approximately 3 mg cm^{-2} for each cathode film, and the electrolyte amount was approximately 0.2 ml (four drops). Galvanostatic cycling tests were performed at room temperature using an Arbin battery tester. GITT measurements were performed by charging/discharging the cell for 270 s at a current density of 200 mA g^{-1} followed by relaxing for 12 h to reach a quasi-equilibrium state. Electrochemically delithiated/lithiated samples were prepared by charging/discharging the cells at a current density of 20 mA g^{-1}, and the charged/discharged cathode films were collected after washing with dimethyl carbonate in an argon-filled glove box.

Characterization. XRD patterns of the as-prepared materials were collected using a Bruker D8 ADVANCE diffractometer (Cu source) in the 2θ range of 15–85°. Rietveld refinement was performed using the PANalytical X'Pert HighScore Plus software. TEM was performed using a Titan X at 200 kV. EDS mappings were taken in STEM mode. SEM images were obtained using a Zeiss Gemini Ultra-55 analytical field-emission scanning electron microscope with acceleration voltages of 5–10 kV.

Hard XAS. Mn K-edge, Cr K-edge, Ti K-edge and Ni K-edge XAS measurements were performed at beamline 20BM at the Advanced Photon Source, Argonne National Laboratory. The measurements were collected in transmission mode using a Si (111) monochromator. Either Mn foil (6,539 eV), Cr foil (5,989 eV), Ti foil (4,966 eV) or Ni foil (8,333 eV) was simultaneously measured during the experiments to calibrate the energy of the individual dataset. All the ex situ samples were sealed between polyimide tapes to avoid air exposure. The XAS spectra were calibrated and normalized using the Athena software package[39,40]. The background contribution was limited below $R_{bkg} = 1.0$ using the built-in AUTOBK algorithm. The normalized spectra were converted from energy to wave-vector **k** and then Fourier transformed from **k**-space to **R**-space. The **R** values should be ~0.3–0.4 shorter than the actual distances because the Fourier transform was not phase corrected[16]. The EXAFS of the Cr edge was analysed using the Artemis software package. The EXAFS fitting was conducted using a Hanning window in k, k^2 and k^3 k-weights simultaneously. The structural models for the fittings were adapted from DFT-calculated structures. The Cr–O and Cr–TM single scattering paths were used to fit the octahedral Cr–O and Cr–TM bonds, respectively. To fit the EXAFS spectra with tetrahedral Cr–O contribution, a Cr–O path (1.65 Å) generated by FEFF calculation was used. The amplitude reduction factor S_0^2 was determined by fitting the Cr foil EXAFS spectrum, and the obtained value (0.7) was used for the fits. k^2-weighted EXAFS spectra are displayed in the figures.

RIXS. The RIXS data were collected at the iRIXS endstation at beamline 8.0.1 at the Advanced Light Source, Lawrence Berkeley National Laboratory. The samples were mounted on a 1 inch copper sample holder and transferred from an argon glove box into the vacuum chamber using a home-made sample transfer kit to avoid any air exposure. Detailed experimental setups and the RIXS data processing have been described previously[41,42].

DEMS measurements. Custom Swagelok cells were used for the DEMS measurements, as described previously[43–45]. The electrolyte, separators and anodes used were identical to those used for the coin-cell tests in this study. The loading density of active material was 14 mg cm^{-2} for the cathode film, and the film was backed by stainless steel mesh to provide the appropriate diameter for electrical contact with the customized current collector. The hermetically sealed cells were assembled in an argon-atmosphere glove box and appropriately attached to the DEMS apparatus to avoid air exposure. The cells were cycled at a current of 20 mA g^{-1} using a Bio-Logic VSP-Series potentiostat under positive Ar pressure (approximately 1.2 bar). During electrochemical cycling, the gas evolution was monitored using a custom-built DEMS apparatus, as described in a previous report[43].

Computational methods. To evaluate the equilibrium ordering in the multicomponent DRX compounds, we constructed a cluster-expansion Hamiltonian in the configurational space of $LiMnO_2$–$LiCrO_2$–Li_2TiO_3 on a rocksalt lattice. The cluster-expansion technique is used to study the configurational thermodynamics of materials in which sites can be occupied by multiple cations, and has been applied to study Li-vacancy configuration in layered materials[46]. As in the $LiMnO_2$–$LiCrO_2$–Li_2TiO_3 system, the cation fcc lattice can be occupied by Li^+–Ti^{4+}–Mn^{3+}–Cr^{3+}. We fit a cluster-expansion model consisting of pair interactions up to 7.1 Å, triplet interactions up to 4 Å and quadruplet interactions up to 4 Å based on a primitive cell of the rocksalt structure with $a = 3$ Å. The effective cluster interactions were obtained from L_1-norm regularized linear regression with the best regularization parameter selected to minimize the cross-validation score[47,48]. Finally, the root mean squared cross-validation errors were converged below 8 meV per atom.

Density functional theory (DFT) calculations were performed using the Vienna ab initio simulation package (VASP)[49] using the projector-augmented wave method[50], a plane-wave basis set with an energy cut-off equal to 520 eV and a reciprocal space discretization of 25 k-points per Å. All calculations were converged to 10^{-6} eV in total energy for electronic loops and 0.02 eV Å^{-1} in interatomic forces for ionic loops. We relied on the Perdew–Burke–Ernzerhof

(PBE) generalized gradient approximation (GGA) exchange-correlation functional with rotationally averaged Hubbard U correction (GGA + U) to compensate for the self-interaction error on all TM atoms except titanium[51]. The U parameters were obtained from literature, where they were calibrated to TM oxide formation energies (3.9 eV for Mn and 3.5 eV for Cr)[52]. The GGA + U computational framework is believed to be reliable in determining the formation enthalpies of similar compounds[53].

Monte Carlo simulations on these cluster-expansion Hamiltonians were performed in a canonical ensemble using Metropolis–Hastings sampling on an 8×9×10 supercell (1,440 atoms) of the primitive unit cell of the rocksalt structure. Percolation analysis was completed on these sampled structures using the dribble package[14].

To compare the formation energies of Cr_{oct} and Cr_{tet}, representative MC structures from equilibrium ensemble sampled at $T = 1{,}273$ K were generated with composition $Li_{1.2}Mn_{0.2}Cr_{0.2}Ti_{0.4}O_{2.0}$ to represent the random arrangement of 120 atoms. All Li_3Cr clusters in the Monte Carlo structures were considered for Cr migration because the large electrostatic repulsion[54] between face-sharing tet-Cr and oct-TM prohibits the occupancy of Cr in the tetrahedral site. Starting from the Li_3Cr tetrahedral cluster shown in Supplementary Fig. 13, a tri-vacancy configuration was created by removing the three Li atoms in the Li_3Cr cluster. The energy of the system ($Li_{33}Mn_6Cr_6Ti_{12}O_{60}$) with the Cr atom placed in either the octahedral or tetrahedral site was evaluated. The R2SCAN meta-GGA exchange-correlation functional was used with a reciprocal space discretization of 25 k-points per Å[55]. The SCAN functional is believed to better capture charge transfer due to redox, which would improve the accuracy of energetics involving Li removal[56,57]. All calculations were converged to 10^{-6} eV in total energy for electronic loops and 0.02 eV Å^{-1} in interatomic forces for ionic loops.

The nudged elastic band (NEB) method was used to compute Cr migration barriers[58] based on five images along the path from the octahedral to the tetrahedral site. The octahedral and tetrahedral structures were relaxed with the GGA functional with a convergence threshold of 10^{-6} eV in total energy for electronic loops and 0.02 eV Å^{-1} in interatomic forces for ionic loops. All NEB calculations were performed using GGA without Hubbard U correction to avoid potential convergence issues associated with electron localization at various atomic centres along the migration path[59,60].

Data availability

All data generated and analysed during this study are included in the published article and its Supplementary Information. Source data are provided with this paper.

Received: 30 November 2020; Accepted: 16 March 2021;
Published online: 10 May 2021

References

1. Kang, K., Meng, Y. S., Bréger, J., Grey, C. P. & Ceder, G. Electrodes with high power and high capacity for rechargeable lithium batteries. *Science* **311**, 977–980 (2006).
2. Schougaard, S. B., Bréger, J., Jiang, M., Grey, C. P. & Goodenough, J. B. $LiNi_{0.5+\delta}Mn_{0.5-\delta}O_2$—A high-rate, high-capacity cathode for lithium rechargeable batteries. *Adv. Mater.* **18**, 905–909 (2006).
3. Julien, C. & Nazri, G. A. in *Handbook of Advanced Electronic and Photonic Materials and Devices* (ed. Singh Nalwa, H.) Ch. 3 (Academic Press, 2001).
4. Jacobson, A. J. & Nazar, L. F. Intercalation Chemistry. *Encyclopedia of Inorganic and Bioinorganic Chemistry* https://doi.org/10.1002/9781119951438.eibc0093 (2011).
5. Wu, F. & Yushin, G. Conversion cathodes for rechargeable lithium and lithium-ion batteries. *Energy Environ. Sci.* **10**, 435–459 (2017).
6. Wiaderek, K. M. et al. Comprehensive insights into the structural and chemical changes in mixed-anion FeOF electrodes by using operando PDF and NMR spectroscopy. *J. Am. Chem. Soc.* **135**, 4070–4078 (2013).
7. Yu, H.-C. et al. Designing the next generation high capacity battery electrodes. *Energy Environ. Sci.* **7**, 1760–1768 (2014).
8. Huang, Q. et al. Fading mechanisms and voltage hysteresis in FeF_2–NiF_2 solid solution cathodes for lithium and lithium-ion batteries. *Small* **15**, 1804670 (2019).
9. Hua, X. et al. Comprehensive study of the CuF_2 conversion reaction mechanism in a lithium ion battery. *J. Phys. Chem. C* **118**, 15169–15184 (2014).
10. Bréger, J. et al. Effect of high voltage on the structure and electrochemistry of $LiNi_{0.5}Mn_{0.5}O_2$: a joint experimental and theoretical study. *Chem. Mater.* **18**, 4768–4781 (2006).
11. Li, H. H. et al. Changes in the cation ordering of layered O3 $LixNi_{0.5}Mn_{0.5}O_2$ during electrochemical cycling to high voltages: an electron diffraction study. *Chem. Mater.* **19**, 2551–2565 (2007).
12. Jones, C. D. W., Rossen, E. & Dahn, J. R. Structure and electrochemistry of $Li_xCr_yCo_{1-y}O_2$. *Solid State Ion.* **68**, 65–69 (1994).
13. Lyu, Y. et al. Atomic insight into electrochemical inactivity of lithium chromate ($LiCrO_2$): irreversible migration of chromium into lithium layers in surface regions. *J. Power Sources* **273**, 1218–1225 (2015).
14. Lee, J. et al. Unlocking the potential of cation-disordered oxides for rechargeable lithium batteries. *Science* **343**, 519–522 (2014).
15. Clément, R. J., Lun, Z. & Ceder, G. Cation-disordered rocksalt transition metal oxides and oxyfluorides for high energy lithium-ion cathodes. *Energy Environ. Sci.* **13**, 345–373 (2020).
16. Balasubramanian, M., McBreen, J., Davidson, I. J., Whitfield, P. S. & Kargina, I. In situ X-ray absorption study of a layered manganese-chromium oxide-based cathode material. *J. Electrochem. Soc.* **149**, A176–A184 (2002).
17. Yang, W. & Devereaux, T. P. Anionic and cationic redox and interfaces in batteries: advances from soft X-ray absorption spectroscopy to resonant inelastic scattering. *J. Power Sources* **389**, 188–197 (2018).
18. Dai, K. et al. High reversibility of lattice oxygen redox quantified by direct bulk probes of both anionic and cationic redox reactions. *Joule* **3**, 518–541 (2019).
19. Li, N. et al. Correlating the phase evolution and anionic redox in Co-free Ni-rich layered oxide cathodes. *Nano Energy* **78**, 105365 (2020).
20. Papp, J. K. et al. A comparison of high voltage outgassing of $LiCoO_2$, $LiNiO_2$, and Li_2MnO_3 layered Li-ion cathode materials. *Electrochim. Acta* **368**, 137505 (2021).
21. Renfrew, S. E. & McCloskey, B. D. Residual lithium carbonate predominantly accounts for first cycle CO_2 and CO outgassing of Li-stoichiometric and Li-rich layered transition-metal oxides. *J. Am. Chem. Soc.* **139**, 17853–17860 (2017).
22. Renfrew, S. E. & McCloskey, B. D. Quantification of surface oxygen depletion and solid carbonate evolution on the first cycle of $LiNi_{0.6}Mn_{0.2}Co_{0.2}O_2$ electrodes. *ACS Appl. Energy Mater.* **2**, 3762–3772 (2019).
23. Van der Ven, A. & Ceder, G. Lithium diffusion mechanisms in layered intercalation compounds. *J. Power Sources* **97–98**, 529–531 (2001).
24. Van der Ven, A. Lithium diffusion in layered Li_xCoO. *Electrochem. Solid-State Lett.* **3**, 301 (1999).
25. Urban, A., Lee, J. & Ceder, G. The configurational space of rocksalt-type oxides for high-capacity lithium battery electrodes. *Adv. Energy Mater.* **4**, 1400478 (2014).
26. Reed, J. & Ceder, G. Role of electronic structure in the susceptibility of metastable transition-metal oxide structures to transformation. *Chem. Rev.* **104**, 4513–4534 (2004).
27. Shannon, R. D. Revised effective ionic radii and systematic studies of interatomic distances in halides and chalcogenides. *Acta Crystallogr. A* **32**, 751–767 (1976).
28. Ji, H. et al. Hidden structural and chemical order controls lithium transport in cation-disordered oxides for rechargeable batteries. *Nat. Commun.* **10**, 592 (2019).
29. Nakajima, M. & Yabuuchi, N. Lithium-excess cation-disordered rocksalt-type oxide with nanoscale phase segregation: $Li_{1.25}Nb_{0.25}V_{0.5}O_2$. *Chem. Mater.* **29**, 6927–6935 (2017).
30. Zhu, Z. et al. Gradient Li-rich oxide cathode particles immunized against oxygen release by a molten salt treatment. *Nat. Energy* **4**, 1049–1058 (2019).
31. Wang, Y., Yang, Z., Qian, Y., Gu, L. & Zhou, H. New insights into improving rate performance of lithium-rich cathode material. *Adv. Mater.* **27**, 3915–3920 (2015).
32. Shi, J.-L. et al. High-capacity cathode material with high voltage for Li-ion batteries. *Adv. Mater.* **30**, 1705575 (2018).
33. Li, X. et al. A new type of Li-rich rock-salt oxide $Li_2Ni_{1/3}Ru_{2/3}O_3$ with reversible anionic redox chemistry. *Adv. Mater.* **31**, 1807825 (2019).
34. Hong, J. et al. Metal–oxygen decoordination stabilizes anion redox in Li-rich oxides. *Nat. Mater.* **18**, 256–265 (2019).
35. Kang, K. & Ceder, G. Factors that affect Li mobility in layered lithium transition metal oxides. *Phys. Rev. B* **74**, 94105 (2006).
36. Sathiya, M. et al. Origin of voltage decay in high-capacity layered oxide electrodes. *Nat. Mater.* **14**, 230–238 (2015).
37. Bréger, J., Kang, K., Cabana, J., Ceder, G. & Grey, C. P. NMR, PDF and RMC study of the positive electrode material $Li(Ni_{0.5}Mn_{0.5})O_2$ synthesized by ion-exchange methods. *J. Mater. Chem.* **17**, 3167–3174 (2007).
38. Sun, X., Duffort, V., Mehdi, B. L., Browning, N. D. & Nazar, L. F. Investigation of the mechanism of Mg insertion in birnessite in nonaqueous and aqueous rechargeable Mg-ion batteries. *Chem. Mater.* **28**, 534–542 (2016).
39. Ravel, B. & Newville, M. ATHENA, ARTEMIS, HEPHAESTUS: data analysis for X-ray absorption spectroscopy using IFEFFIT. *J. Synchrotron Radiat.* **12**, 537–541 (2005).
40. Ravel, B. & Newville, M. ATHENA and ARTEMIS: interactive graphical data analysis using IFEFFIT. *Phys. Scr.* **15**, 1007–1010 (2005).
41. Qiao, R. et al. High-efficiency in situ resonant inelastic X-ray scattering (iRIXS) endstation at the advanced light source. *Rev. Sci. Instrum.* **88**, 33106 (2017).
42. Wu, J. et al. Elemental-sensitive detection of the chemistry in batteries through soft X-ray absorption spectroscopy and resonant inelastic X-ray scattering. *JoVE* **134**, e57415 (2018).
43. McCloskey, B. D., Bethune, D. S., Shelby, R. M., Girishkumar, G. & Luntz, A. C. Solvents' critical role in nonaqueous lithium-oxygen battery electrochemistry. *J. Phys. Chem. Lett.* **2**, 1161–1166 (2011).

44. Mccloskey, B. D. et al. Combining accurate O_2 and Li_2O_2 assays to separate discharge and charge stability limitations in nonaqueous Li–O_2 Batteries. *J. Phys. Chem. Lett.* **4**, 2989–2993 (2013).
45. McCloskey, B. D. et al. Twin problems of interfacial carbonate formation in nonaqueous Li–O_2 batteries. *J. Phys. Chem. Lett.* **3**, 997–1001 (2012).
46. Van der Ven, A., Aydinol, M. K., Ceder, G., Kresse, G. & Hafner, J. First-principles investigation of phase stability in Li_xCoO_2. *Phys. Rev. B* **58**, 2975–2987 (1998).
47. van de Walle, A. Multicomponent multisublattice alloys, nonconfigurational entropy and other additions to the Alloy Theoretic Automated Toolkit. *Calphad* **33**, 266–278 (2009).
48. Nelson, L. J., Hart, G. L. W., Zhou, F. & Ozoliņš, V. Compressive sensing as a paradigm for building physics models. *Phys. Rev. B* **87**, 35125 (2013).
49. Kresse, G. & Furthmüller, J. Efficiency of ab-initio total energy calculations for metals and semiconductors using a plane-wave basis set. *Comput. Mater. Sci.* **6**, 15–50 (1996).
50. Kresse, G. & Joubert, D. From ultrasoft pseudopotentials to the projector augmented-wave method. *Phys. Rev. B* **59**, 1758–1775 (1999).
51. Perdew, J. P., Burke, K. & Ernzerhof, M. Generalized gradient approximation made simple. *Phys. Rev. Lett.* **77**, 3865–3868 (1996).
52. Wang, L., Maxisch, T. & Ceder, G. Oxidation energies of transition metal oxides within the GGA-*U* framework. *Phys. Rev. B* **73**, 195107 (2006).
53. Jain, A. et al. Formation enthalpies by mixing GGA and GGA + *U* calculations. *Phys. Rev. B* **84**, 45115 (2011).
54. Reed, J., Ceder, G. & Van Der Ven, A. Layered-to-spinel phase transition in Li_xMnO_2. *Electrochem. Solid-State Lett.* **4**, A78 (2001).
55. Furness, J. W., Kaplan, A. D., Ning, J., Perdew, J. P. & Sun, J. Accurate and numerically efficient r^{2}SCAN meta-generalized gradient approximation. *J. Phys. Chem. Lett.* **11**, 8208–8215 (2020).
56. Sun, J., Ruzsinszky, A. & Perdew, J. P. Strongly constrained and appropriately normed semilocal density functional. *Phys. Rev. Lett.* **115**, 36402 (2015).
57. Kitchaev, D. A. et al. Energetics of MnO_2 polymorphs in density functional theory. *Phys. Rev. B* **93**, 45132 (2016).
58. Henkelman, G. & Jónsson, H. Improved tangent estimate in the nudged elastic band method for finding minimum energy paths and saddle points. *J. Chem. Phys.* **113**, 9978–9985 (2000).
59. Urban, A., Seo, D.-H. & Ceder, G. Computational understanding of Li-ion batteries. *NPJ Comput. Mater.* **2**, 16002 (2016).
60. Asari, Y., Suwa, Y. & Hamada, T. Formation and diffusion of vacancy-polaron complex in olivine-type $LiMnPO_4$ and $LiFePO_4$. *Phys. Rev. B* **84**, 134113 (2011).

Acknowledgements

This work was supported by the Assistant Secretary for Energy Efficiency and Renewable Energy, Vehicle Technologies Office, under the Applied Battery Materials Program of the US Department of Energy under contract no. DE-AC02-05CH11231. The XAS measurements were performed at the Advanced Photon Source at Argonne National Laboratory, which is supported by the US Department of Energy under contract no. DE-AC02-06CH11357. Work at the Advanced Light Source was supported by the US DOE Office of Science User Facility under contract no. DE-AC02-05CH11231. Work at the Molecular Foundry was supported by the Office of Science, Office of Basic Energy Sciences, of the US Department of Energy under contract no. DE-AC02-05CH11231. The computational analysis was performed using computational resources sponsored by the US Department of Energy's Office of Energy Efficiency and Renewable Energy and located at the National Renewable Energy Laboratory, as well as computational resources provided by the Extreme Science and Engineering Discovery Environment (XSEDE), supported by National Science Foundation grant no. ACI1053575, and the National Energy Research Scientific Computing Center (NERSC), a DOE Office of Science User Facility supported by the Office of Science and the US Department of Energy under contract no. DE-AC02-05CH11231. We thank H. Kim and Z. Lun for assistance with the XAS measurements.

Author contributions

J.H. and G.C. planned the project. G.C. supervised all aspects of the research. J.H. synthesized, characterized and electrochemically tested the proposed materials. With help from M.B., J.H. also analysed the ex situ XAS data. P.Z. performed the theoretical calculations and analysed the results. D.-H.K. performed the TEM characterization. Y.H. collected and analysed the RIXS data with W.Y. With input from B.D.M., M.J.C. collected and analysed the DEMS data. Y.T. performed the SEM characterization. The manuscript was written by J.H. and G.C. and was revised by the other co-authors. All the authors contributed to discussions.

Competing interests

The authors declare no competing interests.

Additional information

Supplementary information The online version contains supplementary material available at https://doi.org/10.1038/s41560-021-00817-6.

Correspondence and requests for materials should be addressed to G.C.

Peer review information *Nature Energy* thanks Naoaki Yabuuchi, Yujie Zhu and the other, anonymous, reviewer(s) for their contribution to the peer review of this work.

Reprints and permissions information is available at www.nature.com/reprints.

Publisher's note Springer Nature remains neutral with regard to jurisdictional claims in published maps and institutional affiliations.